First-principles study on thermoelectric transport properties of Ca_3Si_4

Shin Yabuuchi,* Yosuke Kurosaki, Akinori Nishide, Naoto Fukatani, and Jun Hayakawa
Center for Exploratory Research, Hitachi Ltd., 1-280 Higashi-Koigakubo, Kokubunji-shi, Tokyo 185-8601, Japan
(Received 31 March 2017; revised manuscript received 16 June 2017; published 28 September 2017)

Thermoelectric properties of a semiconducting silicide, Ca_3Si_4, were investigated by first-principles calculations. The calculation results revealed that Ca_3Si_4 has a relatively low lattice thermal conductivity of around 1.2 $Wm^{-1}K^{-1}$ at 800 K. The Seebeck coefficients and the electrical conductivities of Ca_3Si_4 were evaluated by using the Boltzmann transport equation with an energy-dependent relaxation time under the assumption of electron scattering by acoustic phonons. The Seebeck coefficient of n-type Ca_3Si_4 along the x axis is larger than that along the z axis, while the Seebeck coefficient of p-type Ca_3Si_4 along the x axis is smaller than that along the z axis. The electrical conductivity of p-type Ca_3Si_4 is higher than that of n-type Ca_3Si_4 owing to the smaller effective mass of holes, which results in the higher power factor of p-type Ca_3Si_4. Maximum ZT (a dimensionless figure of merit) of single-crystalline p-type Ca_3Si_4 is higher than that of n-type Ca_3Si_4, reaching 0.9 at 800 K. Grain-size effects on the lattice thermal conductivities and power factors were also investigated. Reducing lattice thermal conductivities overcomes the decrease of electrical conductivities and thereby enhances ZT, taking maximum of 1.0 for n-type Ca_3Si_4 and 1.5 for p-type Ca_3Si_4 when the grain size is 10 nm.

DOI: 10.1103/PhysRevMaterials.1.045405

I. INTRODUCTION

Recently, thermoelectric materials have attracted much interest because thermoelectric modules incorporating them can directly convert wasted heat into electric energy. The efficiency of thermoelectric materials is measured by a dimensionless figure of merit, $ZT = S^2\sigma T/(\kappa_l + \kappa_e)$, where S is Seebeck coefficient, σ is electrical conductivity, T is temperature, and κ_l and κ_e are lattice thermal conductivity and electronic thermal conductivity, respectively. For practical use of thermoelectric materials, a value of ZT exceeding 1.0 is desirable, and various bulk materials, such as Skutterudite, clathrates, Heusler alloys, chalcogenides, Zintl phases, and silicides, have been investigated [1–7]. However, in many cases, their toxicity, scarcity, and high cost prevent their practical use. Among a variety of materials, silicide semiconductors such as Mg_2Si, β-$FeSi_2$, and $MnSi_{1.7}$ are expected to be promising candidates because their constituent elements are environmentally friendly, abundant, and nontoxic [8–13]. Thermoelectric properties of Mg_2Si have been extensively studied while silicides with alkaline-earth metals (calcium, strontium, and barium) have been less studied. In the Ca-Si system, several compounds, namely, Ca_2Si,Ca_5Si_3, CaSi, Ca_3Si_4, $Ca_{14}Si_{19}$, and $CaSi_2$, exist [14]. Only Ca_2Si and Ca_3Si_4 are reported to have semiconducting properties, while the others are metal or semimetal [15–24]. Ca_2Si is a direct-band-gap semiconductor, while Ca_3Si_4 has been predicted as a semiconductor with an indirect band gap and its optical, electronic, elastic, and thermophysical properties have also been investigated by first-principles calculations [24–26]. Although there are a few experimental reports on Ca_3Si_4 [14,27], the thermoelectric properties have not been clarified. For improving thermoelectric properties, reducing thermal conductivity is essential. The crystal structure of Ca_3Si_4 (having 42 atoms in a primitive unit cell as shown in Fig. 1) could cause low lattice thermal conductivity owing to its complexity. Due to the anharmonic nature, however, accurately calculating lattice thermal conductivity is still challenging. There are several ways to calculate lattice thermal conductivity by using the Boltzmann transport equation (BTE), equilibrium molecular dynamics (MD) with the Green-Kubo formula, and nonequilibrium MD [28–31]. Recently, lattice thermal conductivities were successfully evaluated from first-principles calculations by using anharmonic interatomic-force constants (IFCs) [28–34]. As for this calculation method, anharmonic IFCs are extracted by fitting a set of Hellmann-Feynman forces acting on atoms in displaced configurations, and they are then used to calculate lattice thermal conductivities.

In this study, the semiconducting silicide Ca_3Si_4 was focused on as a candidate thermoelectric material. Its lattice thermal conductivities were investigated by first-principles calculations and BTE within a relaxation-time approximation considering three-phonon interactions. Seebeck coefficient, electrical conductivity, and power factors of Ca_3Si_4 were evaluated by first-principles calculations and BTE, where electron-relaxation time was obtained from a single-parabolic-band (SPB) model with acoustic-phonon scattering [35–37]. ZT values of Ca_3Si_4 and grain-size effects on the thermoelectric properties were also evaluated.

II. PHONON PROPERTIES AND LATTICE THEMAL CONDUCTIVITY

A. Methodology

To obtain the phonon properties of Ca_3Si_4, first-principles calculation based on density-functional theory (DFT) under the generalized gradient approximation (GGA) was performed by using the Vienna *Ab initio* Simulation Package (VASP) [38,39]. In the calculation, projector-augmented-wave pseudopotentials were used [40]. The lattice parameter of Ca_3Si_4 was optimized with a $5 \times 5 \times 3$ Monkhorst-Pack k-sampling grid and cut-off energy of 500 eV. Precision of total energy convergence during relaxation was as high as 10^{-9}eV. The convergence criterion for the forces on atoms was 10^{-6}eV/Å. The relaxed lattice constants, namely, $a = 8.552$

*shin.yabuuchi.xj@hitachi.com

 ©2017 American Physical Society

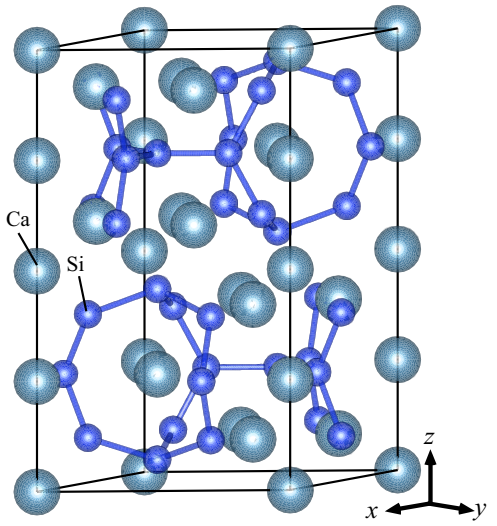

FIG. 1. Crystal structure of Ca_3Si_4.

and $c = 14.91$ Å, agree well with previously reported ones [14,24]. The harmonic and cubic IFCs in real space were computed by taking the finite-displacement approach using the program package Anharmonic Lattice Model (ALAMODE) [31,32]. Cut-off radii of $10.0a_0$ and $8.5a_0$ (where a_0 is Bohr radius) were used for harmonic and cubic IFCs, respectively. The harmonic IFCs within the cut-off radius of $10.0a_0$ include interaction pairs up to the 20th nearest neighbors, resulting in 344 independent parameters. The cubic IFCs within a cut-off radius of $8.5a_0$ result in 1714 independent parameters. The convergence of the dependence of cut-off radius on phonon-band dispersion and mode Grüneisen parameters was checked. The relaxation time of phonons was determined by using the imaginary part of the phonon self-energy under the assumption of the lowest-order three-phonon process with the anharmonic IFCs as input. The detailed computation of the IFCs is described in detail in Ref. [31]. Lattice thermal conductivity was also determined by phonon BTE within the single-mode relaxation-time approximation. A $22 \times 22 \times 12$-$\boldsymbol{q}$-point sampling grid was used for the phonon BTE. To evaluate the phonon-scattering effect of grain boundaries, phonon-relaxation time was estimated by using Matthiessen's rule including boundary scattering rate $2v/L$, where v is phonon group velocity and L is grain size.

B. Phonon dispersion and density of states

Phonon dispersion of Ca_3Si_4 is shown in Fig. 2(a). The acoustic-phonon group velocities in the Γ-M direction are found to be 6500 m/s for a longitudinal-acoustic (LA) phonon and 3450 and 3900 m/s for transversal acoustic (TA) phonons, while the group velocities in the Γ-A direction are 6600 m/s for a LA phonon and 3520 m/s for TA phonons, respectively, in agreement with a previous study [26]. Total phonon density of states (DOS) and partial DOS of Ca_3Si_4 are shown in Fig. 2(b). In the low-frequency range below 70 cm^{-1}, the contribution of calcium (Ca) atoms and silicon (Si) atoms to the DOS is the same level because of the acoustic phonon's nature. In frequency range around 150 cm^{-1}, partial DOS of Ca atoms is larger than that of Si atoms, while above the frequency of 220 cm^{-1}, partial DOS of Si atoms is larger than that of Ca atoms. Figures 2(c) and 2(d) also show the partial DOS of various kinds of Ca and Si sites. The crystal Ca_3Si_4 has four kinds of Wyckoff positions of both Ca sites ($2a$,$2b$,$2c$,$12i$) and Si sites ($2d$,$4f$,$6h$,$12i$). The contribution to the DOS from Ca and Si atoms at different Wyckoff positions is shown in Figs. 2(c) and 2(d). The peak of partial DOS of the Ca atom at Wyckoff positions of $2a$ has the lowest frequency, which is attributed to smaller IFCs compared to that of other Ca sites [41].

C. Lattice thermal conductivity

Temperature dependence of lattice thermal conductivity of intrinsic Ca_3Si_4 and that of Ca_3Si_4 with grain sizes of

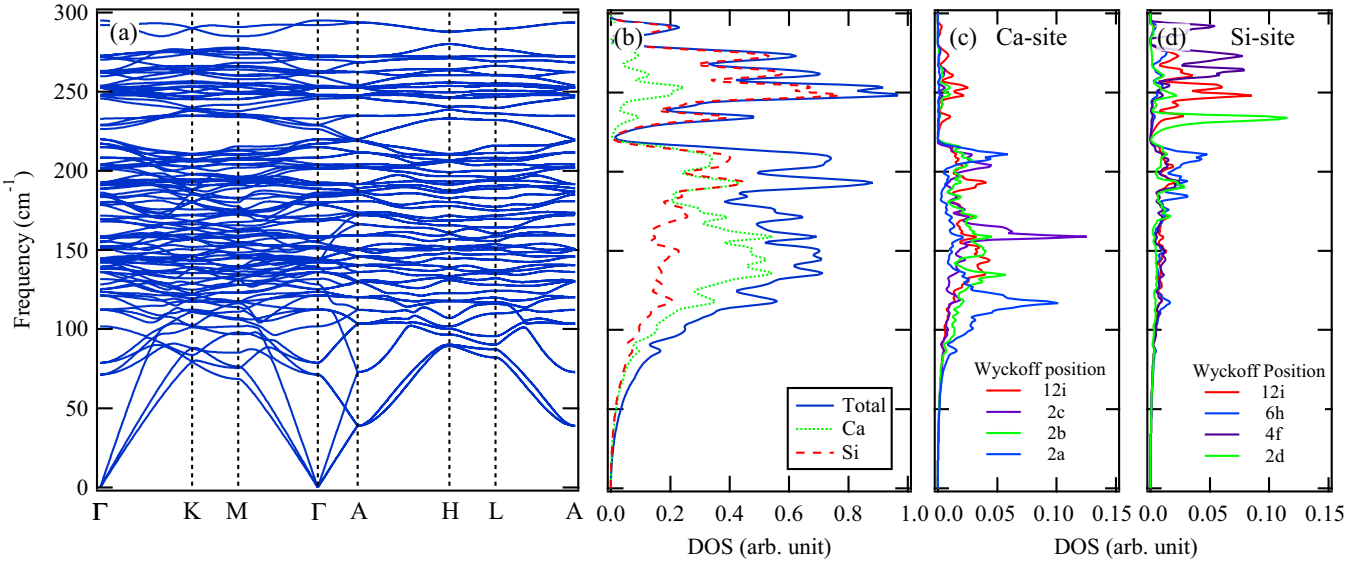

FIG. 2. (a) Phonon dispersion of Ca_3Si_4. (b) Total and partial phonon density of states, and partial phonon density of states of (c) Ca sites and (d) Si sites.

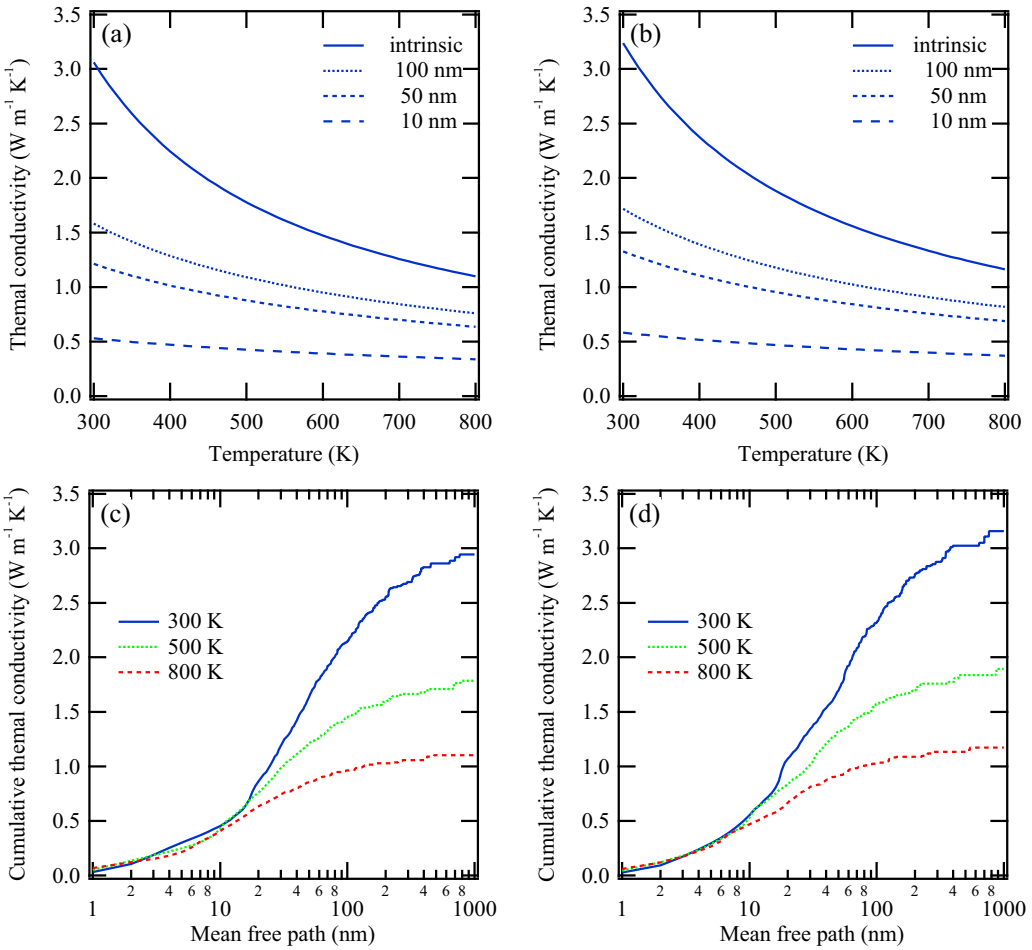

FIG. 3. Temperature dependence of lattice thermal conductivities of intrinsic Ca_3Si_4 and that of Ca_3Si_4 with grain sizes of 100, 50, and 10 nm along the (a) x axis and (b) z axis. Cumulative lattice thermal conductivity of Ca_3Si_4 at 300, 500, and 800 K along the (c) x axis and (d) z axis.

100, 50, and 10 nm along the x and z axes are shown in Figs. 3(a) and 3(b), respectively. Intrinsic lattice thermal conductivities in both the x and z directions reach around 1.2 $W\,m^{-1}K^{-1}$ at 800 K. The difference between the intrinsic lattice thermal conductivities along the x axis and z axis is small, so the conductivity is almost isotropic due to the small anisotropy of phonon group velocities. The values are lower than that of $MnSi_{1.7}$ owing to the complicated crystal structure of Ca_3Si_4 [12]. The intrinsic lattice thermal conductivities also show temperature dependence; they are approximately proportional to inverse temperature $1/T$. Such temperature dependence is known as a common behavior of crystals in the high-temperature regime (in which phonon-phonon scattering is dominant) [29,42]. In terms of the grain-size dependence, the lattice thermal conductivities decrease due to grain-boundary phonon scattering with decreasing grain size. In particular, they are reduced to less than 0.5 $W\,m^{-1}K^{-1}$ at 800 K when the grain size is 10 nm. As the grain size decreases, the temperature dependence weakens and deviates from $1/T$, because grain-boundary scattering becomes dominant. To understand the above grain-size effect quantitatively, the cumulative directional lattice thermal conductivity was analyzed with respect to the mean free path of phonons. Figures 3(c) and 3(d) show the cumulative lattice thermal conductivities of Ca_3Si_4 along the x and z axes, respectively. The mean free paths corresponding to 50% of the cumulative lattice thermal conductivities along the x and z axes at 300, 500, and 800 K are 43, 26, and 16 nm, respectively. In fact, at 300 K, the lattice thermal conductivities of Ca_3Si_4 with grain size of 50 nm are approximately equal to half that of intrinsic Ca_3Si_4. The phonons with mean free paths of less than 50 nm contribute to about half of the total lattice thermal conductivities at 300 K, while about half of the phonons are well scattered by the grain boundary.

To further understand the relationship between phonon properties and lattice thermal conductivities, phonon-scattering rates, phase spaces for three-phonon-scattering processes, mean-free-path distributions, and contributions of phonon modes to lattice thermal conductivity were calculated with respect to frequency. Scattering rates are plotted with respect to frequency in Fig. 4(a). Below a frequency of 50 cm^{-1}, the scattering rate of phonon (acoustic phonon) modes exhibit ω^2 dependence, which is in good agreement with Klemens' formula and other calculations [30,43]. In this calculation, the scattering rate of phonon mode q is

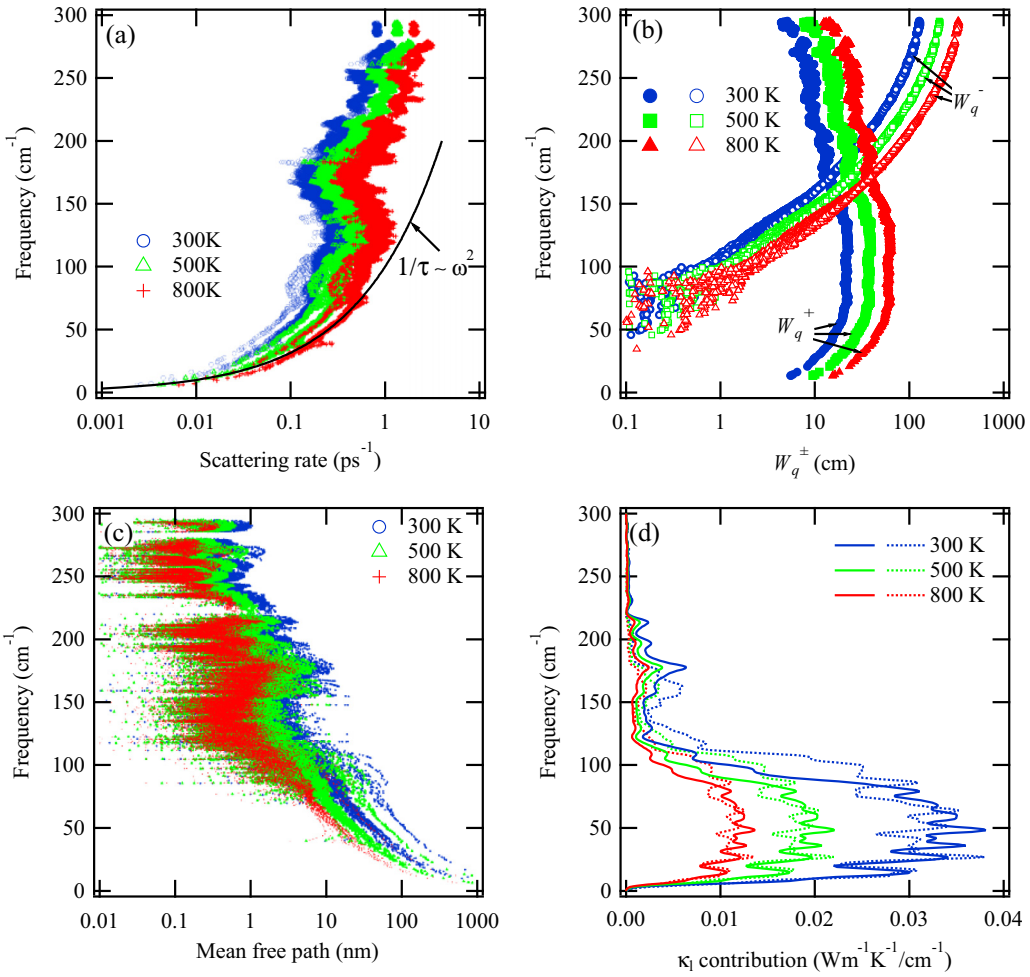

FIG. 4. (a) Scattering rates, (b) energy- and momentum-conserving phase space for three-phonon-scattering processes, (c) mean free paths, and (d) contribution of phonon modes to the lattice thermal conductivities of Ca_3Si_4 along the x and z axes (solid and dashed lines) with respect to frequency.

given as [44]

$$\frac{1}{\tau_p} = \frac{\pi}{N}\sum_{q',q''} |V_3(-q,q',q'')|^2 \times [(n_{q'} + n_{q''} + 1)\delta(\omega - \omega_{q'} - \omega_{q''}) - 2(n_{q'} - n_{q''})\delta(\omega - \omega_{q'} + \omega_{q''})] \quad (1)$$

where ω_q is the phonon frequency, N is the number of $\boldsymbol{q}$ points, and n_q is the Bose-Einstein distribution function. V_3 is the matrix element for three-phonon interaction, which measures the strength of the scattering events. Energy- and momentum-conserving phase space for three-phonon-scattering processes is given as

$$W_q^{\pm} = \frac{1}{N}\sum_{q',q''} \begin{Bmatrix} n_{q''} - n_{q'} \\ n_{q'} + n_{q''} + 1 \end{Bmatrix} \delta(\omega_q - \omega_{q'} \pm \omega_{q''}), \quad (2)$$

where W_q^+ and W_q^- are the phase spaces corresponding to absorption and emission of phonon mode q, respectively. We use the variable q defined by $q = (\boldsymbol{q}, j)$ and $-q = (-\boldsymbol{q}, j)$ where $\boldsymbol{q}$ is the crystal momentum and j is the branch index of phonons. As shown in Fig. 4(b), the phase spaces do not show ω^2 dependence so that the low scattering rates of acoustic-phonon modes are attributed to not only phase spaces but also small values of three-phonon scattering matrix elements. In high-frequency range, the scattering rates are much larger than that of acoustic-phonon modes. The phase spaces of emission of high-frequency phonons (above a frequency of 200 cm^{-1}) also increase with increasing frequency. The large phase spaces contribute to high scattering rates in high-frequency range. The mean free paths of low-frequency phonons are much longer than those of high-frequency phonons as shown in Fig. 4(c). As a result of short mean free paths in high-frequency range above 200 cm^{-1}, as shown in Fig. 4(d), high-frequency phonons hardly contribute as heat carriers.

The phonon properties of Ca_3Si_4 are interesting because it is preferable to reduce the lattice thermal conductivities by nanostructuring compared to semiconductors such as PbTe and PbSe having lattice thermal conductivities of 1.7–2.2 W m^{-1}K^{-1} at 300 K [45]. The previous report has shown that phonons of PbTe with a mean free path smaller than 10 nm comprise about 90% of the lattice thermal conductivity. On the other hand, phonons of Ca_3Si_4 with a mean free path smaller than 10 nm comprise about less than 20% and the majority of phonons have longer mean free paths. In Ca_3Si_4, the contribution of high-frequency phonons (optical phonons)

to the lattice thermal conductivity is small owing to the high scattering rates, therefore the acoustic phonons are dominant heat carriers in Ca_3Si_4 which enables them to be scattered by the grain boundary.

III. ELECTRONIC PROPERTIES

A. Methodology

The electronic structure and transport properties of Ca_3Si_4 were obtained by first-principles calculations (based on the DFT within the GGA) using the OPENMX code [46–48]. Norm-conserving pseudopotentials generated with multiple reference energies and a linear combination of pseudoatomic orbitals (PAOs) were used for the basis set [49]. The PAO basis functions are specified as Ca9.0-$s3p3d1$ and Si7.0-$s3p3d1$, where the atomic symbol is followed by the cut-off (Bohr) radius (9.0 or 7.0) in the generation-by-confinement scheme and three primitive orbitals for the s and p orbitals and one primitive orbital for the d orbital. Real-space grids are used with cut-off energies of 500 Ry in numerical integrations and the solution to the Poisson equation using fast Fourier transform. k-point samplings of $15 \times 15 \times 7$ are used for self-consistent calculation, and those of $45 \times 45 \times 25$ are used for evaluating Seebeck coefficients and electrical conductivities [50]. Electron-relaxation times considering acoustic phonons scattering for many materials have been estimated by using the SPB model [35–37]. In this study, electrical conductivities and Seebeck coefficients are evaluated by using the BTE with an energy (ε)-dependent relaxation time (τ_{ep}) under the assumption of electron scattering by acoustic phonons and a relaxation time attributed to grain-boundary scattering. The relaxation time attributed to acoustic-phonon scattering is given by

$$\tau_{ep} = \frac{2\pi\hbar^4\rho v_l^2}{(2m^*)^{3/2}E_d^2 k_B T}\varepsilon^{-1/2}, \tag{3}$$

where m^* is single-valley effective mass, E_d is the deformation potential, ρ is mass density, v_l is longitudinal sound velocity, $\hbar$ is the reduced Planck constant, and k_B is the Boltzmann constant. In this study, the group velocity of LA phonons was used as v_l. Effective masses of holes and electrons at the conduction-band minimum and the valence-band maximum were calculated. Values of E_d for holes and electrons were calculated in the same manner as described in Ref. [37]. In the case of evaluating grain-size effect, the electron-relaxation time was estimated by using Matthiessen's rule and boundary scattering rate $v_n(\boldsymbol{k})/L$, where $v_n(\boldsymbol{k})$ is the electron or hole group velocity at wave vector $\boldsymbol{k}$ in the Brillouin zone, n is band index, and L is grain size. To evaluate the Seebeck coefficients at high temperature, it is very important to calculate the band gap accurately. Conventional DFT functionals are known to underestimate band gaps [51]. In the case of silicon, the band gap calculated with the GGA is about half the experimental value, while the Heyd-Scuseria-Ernzerhof (HSE) hybrid function well reproduces the band gap of silicon [52]. Accordingly, in this study, the band gap of Ca_3Si_4 was computed with the HSE06 hybrid functional by using VASP [52–55]. A scissors operation was performed to fix the band gap at the value obtained by VASP with HSE06; namely, all the calculated conduction bands by the OPENMX code are shifted up, uniformly, in reciprocal space. To calculate the dependence of doping concentration on Seebeck coefficients and electrical conductivities, Fermi levels (which account for additional electrons for n-type Ca_3Si_4 and reduced electrons for p-type Ca_3Si_4) at given temperature are determined. This definition of Fermi levels is similar to that determined by taking into account activated dopant concentration in semiconductors.

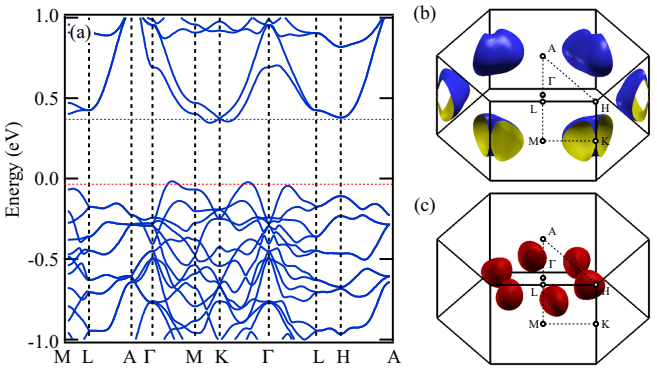

FIG. 5. (a) Electronic band structure of Ca_3Si_4, and Fermi surfaces (b) for n-type Ca_3Si_4 and (c) for p-type Ca_3Si_4.

B. Electronic band structure

The electronic band structure of Ca_3Si_4 is shown in Fig. 5(a). The Fermi surface (constant energy surface) of n-type and p-type Ca_3Si_4 are shown in Figs. 5(b) and 5(c), respectively. The valence-band top locates in the Γ-M direction, while the conduction-band bottom locates in the M-K direction. From the figures, it is clear that these two bands contribute to the Fermi surface for n-type Ca_3Si_4, while the sixfold degenerate valence bands contribute to the Fermi surface for p-type Ca_3Si_4. The indirect band gap of Ca_3Si_4 is 0.35 eV, which agrees well with previously reported values [24]. The calculated effective masses of holes and electrons are $0.55\,m_0$ and $0.85\,m_0$, respectively, where m_0 is free-electron mass. The band gap was also calculated by using HSE06 hybrid functions, resulting in a band gap of 0.76 eV, which is twice that calculated by using the GGA.

C. Seebeck coefficients

Temperature dependence of the Seebeck coefficients of Ca_3Si_4 with a band gap of 0.76 eV (for various doping concentrations) was calculated under the assumption of a rigid band model. Temperature dependences of Seebeck coefficients of n- and p-type Ca_3Si_4 under various doping concentrations (ranging from $1 \times 10^{18}\text{cm}^{-3}$ to $1 \times 10^{21}\text{cm}^{-3}$) along the x and z axes are shown in Figs. 6(a) and 6(b), respectively. Seebeck coefficients with low doping concentrations show peaks. The peaks are attributed to electron excitation from valence bands to conduction bands by thermal energy at high temperature. This temperature dependence is typical behavior of thermoelectric semiconductors and depends on the band gap [9,50]. The assumption of a constant relaxation time for electrons sometimes leads to an overestimation of the absolute values of the Seebeck coefficient. In fact, this assumption overestimates the relaxation times of high-energy electrons compared to the phonon-limited relaxation times, and the Seebeck coefficients

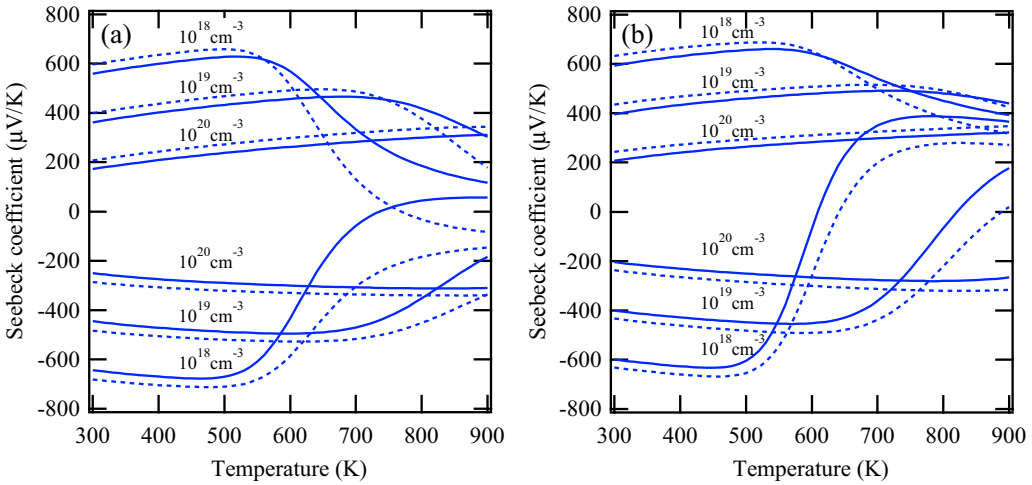

FIG. 6. Temperature dependence of the Seebeck coefficients for n- and p-type Ca_3Si_4 with the band gap of 0.76 eV under various doping concentrations ranging from 1×10^{18}cm^{-3} to 1×10^{21}cm^{-3} along the (a) x axis and (b) z axis. Solid lines are calculated by considering the energy dependence of electron-relaxation time, while dashed lines are calculated by assuming that the relaxation time is constant.

also are overestimated as shown in Figs. 6(a) and 6(b). Thus, to accurately predict Seebeck coefficients, it is essential to consider mode-dependent electron-relaxation time.

Doping-concentration dependences of Seebeck coefficients along the x and z axes (S_{xx} and S_{zz}) of n- and p-type Ca_3Si_4 are shown in Figs. 7(a) and 7(b). The Seebeck coefficients are approximately proportional to the logarithm of doping concentration, except at 800 K. The deviation at 800 K is also attributed to the excitation of electrons from the valence bands to the conduction bands by thermal energy. The absolute values of S_{xx} of n-type Ca_3Si_4 are larger than those of S_{zz}. On the contrary, p-type Ca_3Si_4 shows that the values of S_{zz} are larger than those of S_{xx}. This dependence of Seebeck coefficients on lattice direction reflects the anisotropy of effective masses. In terms of carrier type, the absolute values of the Seebeck coefficients of n-type Ca_3Si_4 are slightly larger than those of p-type Ca_3Si_4 at the same doping concentration, which reflects the difference between the effective masses of electrons ($0.85\,m_0$) and holes ($0.55\,m_0$).

D. Electrical conductivity and power factor

The dependence of electrical conductivities along the x and z axes (σ_{xx} and σ_{zz}) on doping concentration with a band gap of 0.76 eV for n- and p-type Ca_3Si_4 are respectively shown in Figs. 8(a) and 8(b). As doping concentration increases, electrical conductivities monotonically increase (except at 800 K). The deviation from the monotonously increasing behavior at 800 K is due to extra carriers generated by thermal excitations. The values of σ_{xx} for n-type Ca_3Si_4 are larger than those of σ_{zz}. On the other hand, as shown in Fig. 8(b), p-type Ca_3Si_4 shows slightly higher σ_{zz} than σ_{xx}. The directional anisotropy of electrical conductivities also reflects the anisotropy of the group velocity of holes or electrons. The electrical conductivities for p-type Ca_3Si_4 are much higher than those for n-type Ca_3Si_4 at the same doping concentration. The higher electrical conductivity is also attributed to the smaller effective mass of holes ($0.55\,m_0$) than that of electrons ($0.85\,m_0$).

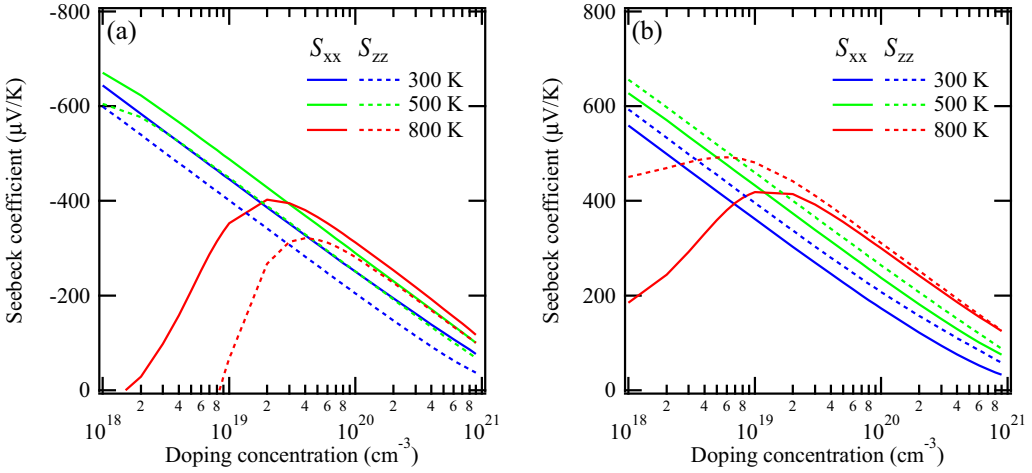

FIG. 7. Seebeck coefficients of Ca_3Si_4 as a function of doping concentration along the x axis and the z axis (S_{xx} and S_{zz}) for (a) n-type and (b) p-type Ca_3Si_4. Solid lines are Seebeck coefficients along the x axis (S_{xx}). Dashed lines are Seebeck coefficients along the z axis (S_{zz}).

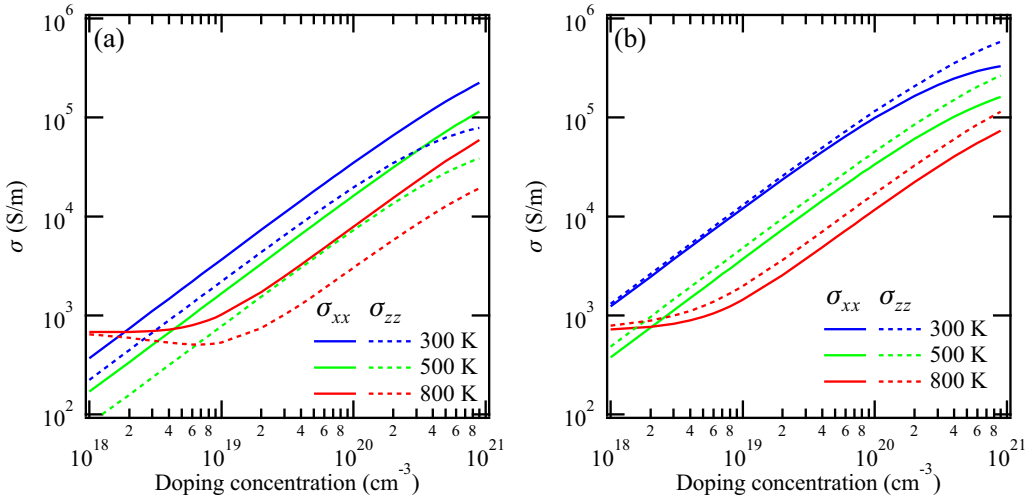

FIG. 8. Electrical conductivities of Ca_3Si_4 as a function of doping concentration along the x and the z axes (σ_{xx} and σ_{zz}) for n-type and (b) p-type Ca_3Si_4. Solid lines are electrical conductivities along the x axis (σ_{xx}). Dashed lines are electrical conductivities along the z axis (σ_{zz}).

The dependences of the power factor along the x and z axes (P_{xx} and P_{zz}) on doping concentration for n- and p-type Ca_3Si_4 are shown in Figs. 9(a) and 9(b), respectively. The maximum power factor at 300 K for n-type Ca_3Si_4 reaches 2.5 mW m^{-1}K^{-2} and decreases with increasing temperature. The maximum power factor for p-type Ca_3Si_4 reaches 5.1 mW m^{-1}K^{-2}, which is twice that for n-type Ca_3Si_4. This difference is mainly attributed to the higher electrical conductivities of p-type Ca_3Si_4 because the difference between the absolute values of the Seebeck coefficients of n-type and p-type Ca_3Si_4 is not large.

The temperature dependence of electrical conductivities (averaged over three directions) of n- and p-type Ca_3Si_4 with a doping concentration of 1×10^{20} cm^{-3} with grain sizes of 50 and 10 nm as well as without grain boundaries are shown in Figs. 10(a) and 10(b). The electrical conductivities of both n-type and p-type Ca_3Si_4 decrease with decreasing grain size. As shown in Fig. 10(a), the electrical conductivity of Ca_3Si_4 with a grain size of 100 nm is almost equal to that without grain boundaries. As grain sizes decreases, the electrical conductivities are reduced due to grain-boundary scattering. When the grain size is 10 nm, the electrical conductivities of n-type Ca_3Si_4 at 300 K decrease to 2.4×10^4 S/m (down 19%), compared to that without grain boundaries. On the other hand, the electrical conductivities of p-type Ca_3Si_4 at 300 K decrease to 6.5×10^4 S/m (down 38%) when the grain size is 10 nm. The reduction in electrical conductivities of p-type Ca_3Si_4 is remarkable. This is due to the longer mean free path of holes compared with that of electrons. Consequently, the electrical conductivities of p-type Ca_3Si_4 tend to be more affected by grain-boundary scattering compared with n-type Ca_3Si_4.

The temperature dependences of the power factors of n- and p-type Ca_3Si_4 with a doping concentration of 1×10^{20} cm^{-3} and grain sizes of 50 and 10 nm as well as without grain boundaries are shown in Figs. 11(a) and 11(b). The power factors are averaged over three directions. The power factors

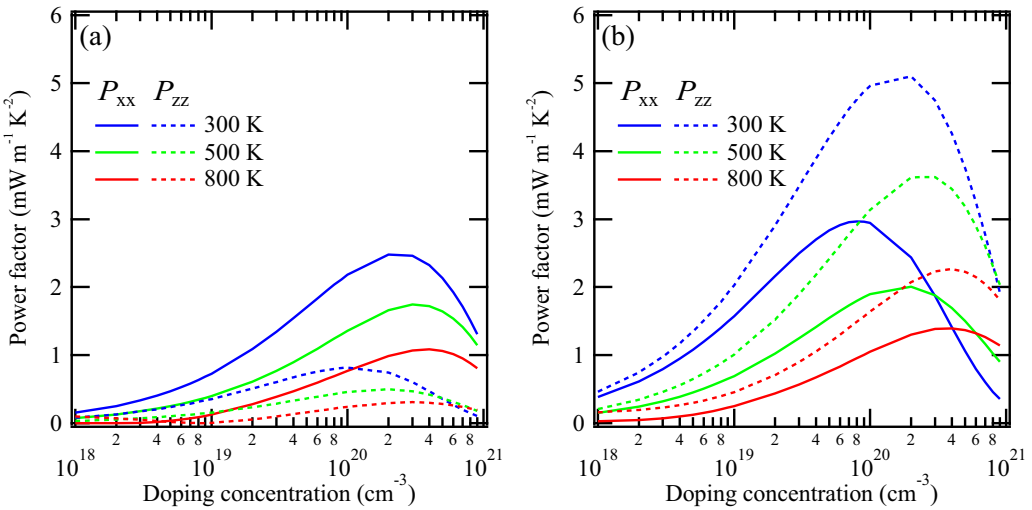

FIG. 9. Power factors of Ca_3Si_4 as a function of doping concentration along the x and z axes (P_{xx} and P_{zz}) for n-type and (b) p-type Ca_3Si_4. Solid lines are power factors along the x axis (P_{xx}). Dashed lines are power factors along the z axis (P_{zz}).

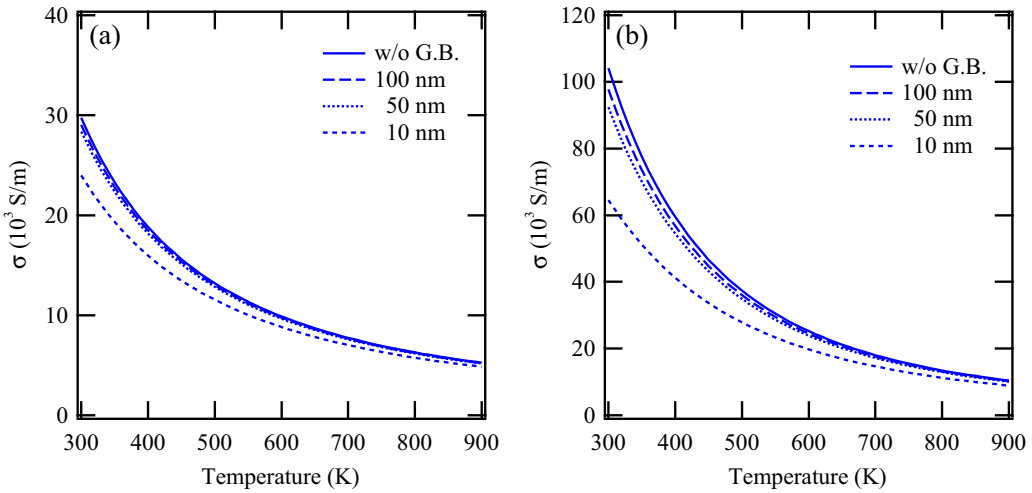

FIG. 10. Temperature dependences of electrical conductivities of Ca_3Si_4 with doping concentration of 1×10^{20} cm^{-3} without grain boundary and with grain sizes of 100, 50, and 10 nm along the (a) x axis and (b) z axis.

also decrease with decreasing grain size, and the grain-size effect on the power factor is similar to that of electrical conductivity. In the case of n-type Ca_3Si_4 with a grain size of 10 nm, compared to the power factors without grain boundaries, the power factors at 300 K decrease to 1.4 mW m^{-1}K^{-2} (down 19%). These decrease rates of power factors are similar to those of electrical conductivity, because the Seebeck coefficient of Ca_3Si_4 with a grain size of 10 nm is similar to that in the case without grain boundaries (not shown in the figures).

E. Dimensionless figure of merit

The dependences of ZT values of n- and p-type Ca_3Si_4 on doping concentration were evaluated. Electronic thermal conductivity was evaluated by using the Wiedemann-Franz law, $\kappa_e = L\sigma T$, where $L(=2.44 \times 10^{-8}\mathrm{W}\,\Omega\,\mathrm{K}^{-1})$ is Lorentz number. The dependences of ZT along the x and z axes (ZT_x and ZT_z) on the doping concentration of n- and p-type Ca_3Si_4 are shown in Figs. 12(a) and 12(b), respectively. Maximum ZT values with respect to doping concentration increase with increasing temperature, although the maximum power factor and electrical conductivities decrease with increasing temperature, as shown in Figs. 8 and 9. The n-type Ca_3Si_4 shows maximum ZT of 0.59 along the x axis at 800 K, while maximum ZT of p-type Ca_3Si_4 is 0.92 along the z axis at the same doping concentration. The anisotropy of maximum ZT corresponds to the behavior of the power factors, since lattice thermal conductivity of Ca_3Si_4 is almost isotropic.

To estimate the ZT values of polycrystalline Ca_3Si_4 with nanograins, the power factors and thermal conductivities are averaged over three directions. The dependences of ZT values of n- and p-type Ca_3Si_4 (with a grain size of 10 nm) on doping concentration are shown in Figs. 12(c) and 12(d), respectively. Maximum ZT of n-type Ca_3Si_4 reaches 1.0 at 800 K. The p-type Ca_3Si_4 with a grain size of 10 nm shows maximum ZT of 1.5 at 800 K. The enhancement of ZT is achieved by small grain size because reducing the lattice thermal conductivities overcomes the decrease of the electrical conductivities. These

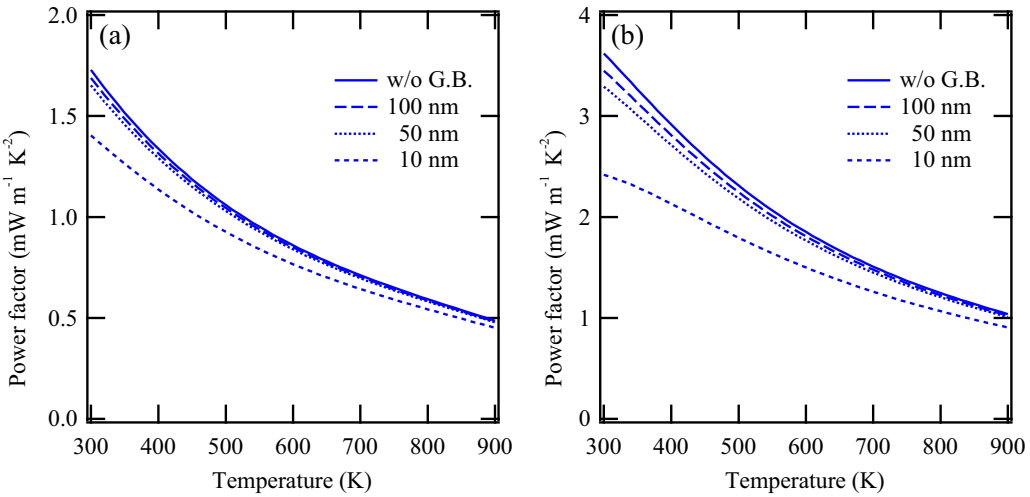

FIG. 11. Temperature dependences of power factors of Ca_3Si_4 with doping concentration of 1×10^{20} cm^{-3} without grain boundaries and with grain sizes of 100, 50, and 10 nm for (a) n-type and (b) p-type Ca_3Si_4.

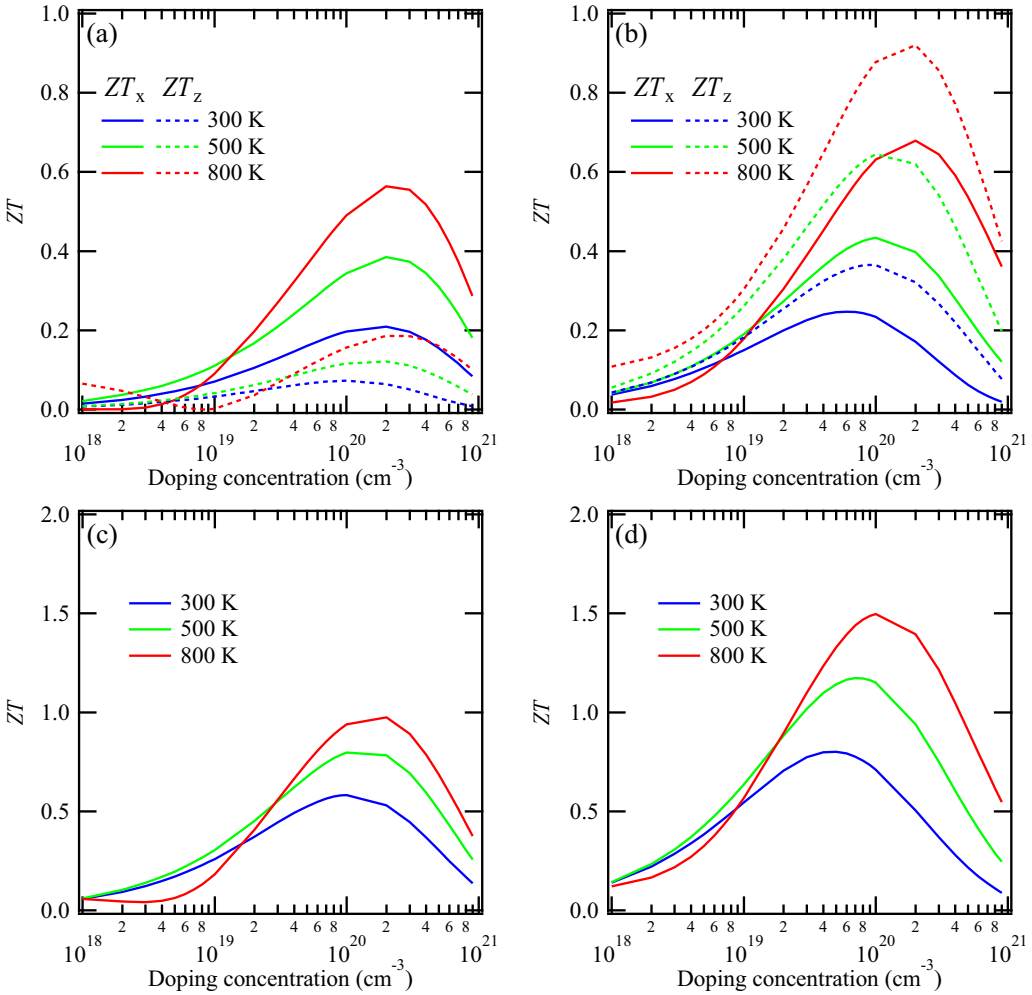

FIG. 12. ZT values of Ca_3Si_4 along the x axis (ZT_x) and the z axis (ZT_z) for (a) n-type and (b) p-type Ca_3Si_4 as a function of doping concentration. ZT values of Ca_3Si_4 with the grain size of 10 nm for (c) n-type and for (d) p-type Ca_3Si_4 as a function of doping concentration.

ZT values indicate that Ca_3Si_4 is a potential candidate for an environmentally friendly thermoelectric material with high ZT.

The above discussions are somewhat simplistic in clarifying the precise thermoelectric properties of Ca_3Si_4. Acoustic-phonon scattering and grain-boundary scattering were only taken into account to evaluate the electron-relaxation time of Ca_3Si_4. Electron-phonon interaction, electron-electron interactions, and interfacial structures at grain boundary could also affect electron-relaxation time as well as phonon-relaxation time. The band gap may have a temperature dependence which affects the thermoelectric properties. We believe that most parts of our calculations are valid. However, some approximations might cause overestimation of ZT. In the future, to verify thermoelectric properties of Ca_3Si_4, it is necessary to compare with experimental measurements and some other methods.

IV. CONCLUSIONS

Thermoelectric properties, namely, phonon properties, thermal conductivity, electronic structure, electrical conductivity, and Seebeck coefficient, of a semiconducting silicide (Ca_3Si_4) were investigated by first-principles calculations. The calculation showed following results Ca_3Si_4 has a low lattice thermal conductivity of around 1.2 $Wm^{-1}K^{-1}$ at 800 K. The Seebeck coefficient of n-type Ca_3Si_4 along the x axis is larger than that along the z axis, while the Seebeck coefficient of p-type Ca_3Si_4 along the x axis is smaller than that along the z axis. The electrical conductivity of p-type Ca_3Si_4 is higher than that of n-type Ca_3Si_4 due to the smaller effective mass of holes, which results in a larger power factor of p-type Ca_3Si_4. ZT of single-crystalline n- and p-type Ca_3Si_4 at 800 K reaches 0.59 and 0.92, respectively. Nanostructuring reduces both lattice thermal conductivities and electrical conductivities of Ca_3Si_4. Reducing lattice thermal conductivities overcomes the decrease of electrical conductivities and thereby enhances ZT, taking maximum ZT of 1.0 for n-type Ca_3Si_4 and 1.5 for p-type Ca_3Si_4 when the grain size is 10 nm. These results also indicate that nanostructuring is an effective way to enhance the thermoelectric properties of semiconducting Ca_3Si_4.

ACKNOWLEDGMENTS

This work is based on results obtained from the Future Pioneering Program "Research and Development of Thermal Management and Technology" commissioned by the New

Energy and Industrial Technology Development Organization (NEDO). It is also supported by TherMAT and partially used computational resources of the K computer provided by the RIKEN Advanced Institute for Computational Science through the HPCI System Research project (Project IDs hp150058 and hp160014).

[1] G. Rogl, A. Grytsiv, P. Rogl, N. Peranio, E. Bauer, M. Zehetbauer, and O. Eibl, Acta Mater. **63**, 30 (2014).
[2] T. Takabatake, K. Suekuni, T. Nakayama, and E. Kaneshita, Rev. Mod. Phys. **86**, 669 (2014).
[3] C. Yu, T.-J. Zhu, R.-Z. Shi, Y. Zhang, X.-B. Zhao, and J. He, Acta Mater. **57**, 2757 (2009).
[4] G. Joshi, R. He, M. Engber, G. Samsonidze, T. Pantha, E. Dahal, K. Dahal, J. Yang, Y. Lan, B. Kozinsky, and Z. Ren, Energy Environ. Sci. **7**, 4070 (2014).
[5] L.-D. Zhao, S.-H. Lo, Y. Zhang, H. Sun, G. Tan, C. Uher, C. Wolverton, V. P. Dravid, and M. G. Kanatzidis, Nature (London) **508**, 373 (2014).
[6] H. Liu, X. Shi, F. Xu, L. Zhang, W. Zhang, L. Chen, Q. Li, C. Uher, T. Day, and G. J. Snyder, Nat. Mater. **11**, 422 (2012).
[7] E. S. Toberer, A. Zevalkink, N. Crisosto, and G. J. Snyder, Adv. Funct. Mater. **20**, 4357 (2010).
[8] J.-i. Tani and H. Kido, Physica B **364**, 218 (2005).
[9] M. Akasaka, T. Iida, A. Matsumoto, K. Yamanaka, Y. Takanashi, T. Imai, and N. Hamada, J. Appl. Phys. **104**, 013703 (2008).
[10] A. U. Khan, N. Vlachos, and T. Kyratsi, Scr. Mater. **69**, 606 (2013).
[11] A. Heinrich, H. Griessmann, G. Behr, K. Ivanenko, J. Schumann, and H. Vinzelberg, Thin Solid Films **381**, 287 (2001).
[12] A. Yamamoto, S. Ghodke, H. Miyazaki, M. Inukai, Y. Nishino, M. Matsunami, and T. Takeuchi, Jpn. J. Appl. Phys. **55**, 020301 (2016).
[13] Y. Miyazaki, H. Hamada, K. Hayashi, and K. Yubuta, J. Electron. Mater. **46**, 2705 (2017).
[14] P. Manfrinetti, M. L. Fornasini, and A. Palenzona, Intermetallics **8**, 223 (2000).
[15] J. Evers and A. Weiss, Solid State Commun. **17**, 41 (1975).
[16] J. Evers and A. Weiss, Mater. Res. Bull. **9**, 549 (1974).
[17] T. Inaba, A. Kato, K. Miura, M. Akasaka, T. Iida, Y. Momose, and H. Tatsuoka, Thin Solid Films **515**, 8226 (2007).
[18] G. Gao, N. W. Ashcroft, M. Miao, and R. Hoffmann, J. Phys. Chem. C **118**, 25167 (2014).
[19] G. Vogg, M. S. Brandt, M. Stutzmann, and M. Albrecht, J. Cryst. Growth **203**, 570 (1999).
[20] A. Currao, S. Wengert, R. Nesper, J. Curda, and H. Hillebrecht, Z. Anorg. Allg. Chem. **622**, 501 (1996).
[21] D. B. Migas, L. Miglio, V. L. Shaposhnikov, and V. E. Borisenko, Phys. Rev. B **67**, 205203 (2003).
[22] Z. Yang, D. Shi, B. Wen, R. Melnik, S. Yao, and T. Li, J. Solid State Chem. **183**, 136 (2010).
[23] D. B. Migas, V. O. Bogorodz, A. B. Filonov, V. L. Shaposhnikov, V. E. Borisenko, and N. G. Galkin, Jpn. J. Appl. Phys. **54**, 07JA03 (2015).
[24] D. B. Migas, V. L. Shaposhnikov, A. B. Filonov, N. N. Dorozhkin, and V. E. Borisenko, J. Phys.: Condens. Matter **19**, 346207 (2007).
[25] R. Gao and Q. Xie, Phys. Procedia **11**, 99 (2011).
[26] X. Tao, J. Yang, L. Xi, and Y. Ouyang, J. Solid State Chem. **194**, 179 (2012).
[27] F. Canepa, M. Napoletano, P. Manfrinetti, and A. Palenzona, J. Alloys Compd. **299**, 20 (2000).
[28] K. Esfarjani and H. T. Stokes, Phys. Rev. B **77**, 144112 (2008).
[29] J. Shiomi, K. Esfarjani, and G. Chen, Phys. Rev. B **84**, 104302 (2011).
[30] K. Esfarjani, G. Chen, and H. T. Stokes, Phys. Rev. B **84**, 085204 (2011).
[31] T. Tadano, Y. Gohda, and S. Tsuneyuki, J. Phys.: Condens. Matter **26**, 225402 (2014).
[32] T. Tadano and S. Tsuneyuki, Phys. Rev. B **92**, 054301 (2015).
[33] T. Tadano, Y. Gohda, and S. Tsuneyuki, Phys. Rev. Lett. **114**, 095501 (2015).
[34] A. Togo, L. Chaput, and I. TanakaPhys. Rev. B **91**, 094306 (2015).
[35] A. F. May, E. S. Toberer, A. Saramat, and G. J. Snyder, Phys. Rev. B **80**, 125205 (2009).
[36] P. H. M. Bottger, G. S. Pomrehn, G. J. Snyder, and T. G. Finstad, Phys. Status Solidi A **208**, 2753 (2011).
[37] R. Guo, X. Wang, Y. Kuang, and B. Huang, Phys. Rev. B **92**, 115202 (2015).
[38] G. Kresse and J. Furthmüller, Phys. Rev. B **54**, 11169 (1996).
[39] J. P. Perdew, K. Burke, and M. Ernzerhof, Phys. Rev. Lett. **77**, 3865 (1996).
[40] P. E. Blochl, Phys. Rev. B **50**, 17953 (1994).
[41] We evaluated the IFCs of Ca and Si atoms. The highest force constant of a Ca atom at Wyckoff positions of $2c$ ($0.18\,\mathrm{Ry}/a_0^2$) is more than twice that of $2a$ ($0.07\,\mathrm{Ry}/a_0^2$).
[42] P. Klemens, Proc. R. Soc. A **208**, 108 (1951).
[43] P. G. Klemens, in *Thermal Conductivity*, edited by R. P. Tve (Academic, London, 1969), Vol. 1.
[44] A. A. Maradudin and A. E. Fein, Phys. Rev. **128**, 2589 (1962).
[45] Z. Tian, J. Garg, K. Esfarjani, T. Shiga, J. Shiomi, and G. Chen, Phys. Rev. B. **85**, 184303 (2012).
[46] See http://www.openmx-square.org/
[47] T. Ozaki, Phys. Rev. B. **67**, 155108 (2003).
[48] T. Ozaki and H. Kino, Phys. Rev. B **69**, 195113 (2004).
[49] D. Vanderbilt, Phys. Rev. B **41**, 7892 (1990).
[50] S. Yabuuchi, M. Okamoto, A. Nishide, Y. Kurosaki, and J. Hayakawa, Appl. Phys. Express **6**, 025504 (2013).
[51] J. P. Perdew and M. Levy, Phys. Rev. Lett. **51**, 1884 (1983).
[52] J. Heyd, J. E. Peralta, G. E. Scuseria, and R. L. Martin, J. Chem. Phys. **123**, 174101 (2005).
[53] J. Heyd, G. E. Scuseria, and M. Ernzerhof, J. Chem. Phys. **118**, 8207 (2003); **124**, 219906(E) (2006).
[54] A. V. Krukau, O. A. Vydrov, A. F. Izmaylov, and G. E. Scuseria, J. Chem. Phys. **125**, 224106 (2006).
[55] J. Paier, A. M. Marsman, K. Hummer, and G. Kresse, J. Chem. Phys. **124**, 154709 (2006).